(YL1/2; Serotec), 1:200; chicken anti-betaIV-spectrin[18] (gift from M. Komada), 1:100; 4,6-diamidino-2-phenylindole (DAPI; Sigma), 4 µg ml^{-1}; tetramethylrhodamine β-isothiocyanate (TRITC)–phalloidin (Sigma), 50 ng ml^{-1}. The secondary antibodies were fluorescein isothiocyanate (FITC)-conjugated anti-rabbit IgG, 1:200; TRITC–donkey anti-guinea-pig IgG, 1:200; FITC–donkey anti-chicken IgY, 1:100 (all from Jackson ImmunoResearch); FITC–goat anti-mouse IgG1, 1:200 (Southern Biotech); Alexa Fluor-goat anti-rabbit IgG, 1:100 (Molecular Probes). For western blotting[19], primary antibodies were used at tenfold greater dilutions.

Microscopy and morphometry

Depolymerization of Schwann cell microtubules in sciatic nerve *in vivo* was performed by topical treatment with colchicine as described[20], and microtubules were allowed to reform for 3 days. By 5 days after colchicine treatment the microtubules had reached the paranodes showing that microtubule disruption is completely reversible (data not shown). Teased fibres were prepared from nerves fixed for 1 h in 4% paraformaldehyde, 0.1 M sodium phosphate buffer pH 7.3, and washed in several changes of phosphate buffer. The lengths of quadriceps nerves were measured from spinal cord exit to muscle insertion point. Teased fibres from quadriceps nerves of WT and KO mice were stained with TRITC–phalloidin and DAPI, and 100 internodes and the lengths of two quadriceps nerves were measured for each animal ($n = 3$). For chimaeras, 200 internodal distances were measured for each Schwann cell type ($n = 3$). Nerves were prepared for electron microscopy as described previously[4]. For measurement of *g*-ratios, micrographs of randomly selected fields of ultrathin transverse sections of quadriceps nerves from 3-week-old WT and KO mice ($n = 3$ for each group, 120 fibres per group) were scanned and analysed using NIH Image. The *g*-ratio was calculated and all results are shown as means ± s.e.m. The best fit for the growth rates of internodal and nerve length was found (*F*-test; Prism 3.03) and superimposed on the measured values shown in Fig. 2b. The growth rate of WT internodal length fitted a rectangular hyperbola, whereas the growth rate of KO internodal length fitted a straight line (linear regression). The growth rates of WT and KO nerve length both fitted a rectangular hyperbola. Bright-field images of teased sciatic nerve fibres stained for P0 and MBP mRNA by *in situ* hybridization with digoxigenin-labelled probes[21] were photographically inverted to compare the signal intensity between WT, KO and colchicine-treated WT Schwann cells. Sense probes gave negligible background staining. Images of internodes were normalized by rescaling to a length of 400 pixels and imported into MATLAB software as a two-dimensional matrix representing pixel intensity. A three-dimensional array was created by concatenating individual images in the *Z* dimension. From this array, the mean value of pixel intensity in the *Z* dimension was calculated for each pixel, resulting in a two-dimensional matrix.

Electrophysiology

Quadriceps nerves from 3-week-old KO and WT mice were transferred from oxygenated Krebs solution to an isolated chamber containing an array of Ag/AgCl electrodes with 1-mm intervals and surrounded by liquid paraffin maintained at 37 °C for periods no longer than 10 min. The proximal end of the nerve was excited by a square wave (0.1 ms, 0.1–1.5 V) and the conduction distance was varied from 2 mm to 7 mm by altering the stimulating electrode position. The voltage was adjusted to ensure exact duplication of the active population, and the compound action potential was viewed on a storage oscilloscope. Values were stored as digitized signals with the use of Chart software (MacLab System). Conduction times were measured as described[4].

Behavioural testing

Mice were conditioned to the RotaRod 1 day before the trial, and the RotaRod test was terminated either when the mouse fell from the rod or at 60 s. Four trials per mouse were performed, separated by at least 10 min to avoid exhaustion of the animal. The thresholds and times for hindpaw withdrawal in response to graded mechanical stimulation and thermal stimulus were performed as described[4].

Chimaeras

Chimaeras were obtained by injecting the ES cell line E14Tg2aSc4TP6.3 expressing GFP-tagged tau protein into WT or KO blastocysts[5]. For internodal length measurements in quadriceps nerves, chimaeras were selected with an approximately equal contribution from each Schwann cell type.

1. Brill, M. H., Waxman, S. G., Moore, J. W. & Joyner, R. W. Conduction velocity and spike configuration in myelinated fibres: computed dependence on internode distance. *J. Neurol. Neurosurg. Psychiatry* **40**, 769–774 (1977).
2. Ramón y Cajal, S. *Histology* (Bailliere, Tindall & Cox, London, 1933).
3. Sherman, D. L., Fabrizi, C., Gillespie, C. S. & Brophy, P. J. Specific disruption of a Schwann cell dystrophin-related protein complex in a demyelinating neuropathy. *Neuron* **30**, 677–687 (2001).
4. Gillespie, C. S. *et al.* Peripheral demyelination and neuropathic pain behavior in periaxin-deficient mice. *Neuron* **26**, 523–531 (2000).
5. Pratt, T., Sharp, L., Nichols, J., Price, D. J. & Mason, J. O. Embryonic stem cells and transgenic mice ubiquitously expressing a tau-tagged green fluorescent protein. *Dev. Biol.* **228**, 19–28 (2000).
6. Ainger, K. *et al.* Transport and localization elements in myelin basic protein mRNA. *J. Cell Biol.* **138**, 1077–1087 (1997).
7. Carson, J. H., Worboys, K., Ainger, K. & Barbarese, E. Translocation of myelin basic protein mRNA in oligodendrocytes requires microtubules and kinesin. *Cell Motil. Cytoskeleton* **38**, 318–328 (1997).
8. Colman, D. R., Kreibich, G., Frey, A. B. & Sabatini, D. D. Synthesis and incorporation of myelin polypeptides into CNS myelin. *J. Cell Biol.* **95**, 598–608 (1982).
9. Griffiths, I. R. *et al.* Expression of myelin protein genes in Schwann cells. *J. Neurocytol.* **18**, 345–352 (1989).
10. Anzini, P. *et al.* Structural abnormalities and deficient maintenance of peripheral nerve myelin in mice lacking the gap junction protein connexin 32. *J. Neurosci.* **17**, 4545–4551 (1997).
11. Hursh, J. B. Conduction velocity and diameter of nerve fibers. *Am. J. Physiol.* **127**, 131–139 (1939).
12. Huxley, A. F. & Stampfli, R. Evidence for saltatory conduction in peripheral myelinated nerve fibres. *J. Physiol. (Lond.)* **108**, 315–339 (1949).
13. McIntyre, C. C., Richardson, A. G. & Grill, W. M. Modeling the excitability of mammalian nerve fibers: influence of afterpotentials on the recovery cycle. *J. Neurophysiol.* **87**, 995–1006 (2002).
14. Ranvier, L. Des étranglements annulaires et des segments interannulaires chez les Raies et les Torpilles. *C. R. Acad. Sci.* **75**, 1129–1132 (1872).
15. Hiscoe, H. B. Distribution of nodes and incisures in normal and regenerated nerve. *Anat. Rec.* **99**, 447–475 (1947).
16. Schlaepfer, W. W. & Myers, F. K. Relationship of myelin internode elongation and growth in the rat sural nerve. *J. Comp. Neurol.* **147**, 255–266 (1973).
17. Tait, S. *et al.* An oligodendrocyte cell adhesion molecule at the site of assembly of the paranodal axo-glial junction. *J. Cell Biol.* **150**, 657–666 (2000).
18. Komada, M. & Soriano, P. βIV-spectrin regulates sodium channel clustering through ankyrin-G at axon initial segments and nodes of Ranvier. *J. Cell Biol.* **156**, 337–348 (2002).
19. Gillespie, C. S., Sherman, D. L., Blair, G. E. & Brophy, P. J. Periaxin, a novel protein of myelinating Schwann cells with a possible role in axonal ensheathment. *Neuron* **12**, 497–508 (1994).
20. Trapp, B. D. *et al.* Polarization of myelinating Schwann cell surface membranes: role of microtubules and the trans-Golgi network. *J. Neurosci.* **15**, 1797–1807 (1995).
21. Collinson, J. M., Marshall, D., Gillespie, C. S. & Brophy, P. J. Transient expression of neurofascin by oligodendrocytes at the onset of myelinogenesis: implications for mechanisms of axon-glial interaction. *Glia* **23**, 11–23 (1998).

....

Calcium transients in astrocyte endfeet cause cerebrovascular constrictions

Sean J. Mulligan & Brian A. MacVicar

Brain Research Centre, Department of Psychiatry, University of British Columbia, 2211 Wesbrook Mall, Vancouver, BC, Canada, V6T 2B5

....

Cerebral blood flow (CBF) is coupled to neuronal activity and is imaged *in vivo* to map brain activation[1]. CBF is also modified by afferent projection fibres that release vasoactive neurotransmitters[2,3] in the perivascular region, principally on the astrocyte endfeet[4,5] that outline cerebral blood vessels[6]. However, the role of astrocytes in the regulation of cerebrovascular tone remains uncertain. Here we determine the impact of intracellular Ca^{2+} concentrations ($[Ca^{2+}]_i$) in astrocytes on the diameter of small arterioles by using two-photon Ca^{2+} uncaging[7,8] to increase $[Ca^{2+}]_i$. Vascular constrictions occurred when Ca^{2+} waves evoked by uncaging propagated into the astrocyte endfeet and caused large increases in $[Ca^{2+}]_i$. The vasoactive neurotransmitter noradrenaline[2,3] increased $[Ca^{2+}]_i$ in the astrocyte endfeet, the peak of which preceded the onset of arteriole constriction. Depressing increases in astrocyte $[Ca^{2+}]_i$ with BAPTA inhibited the vascular constrictions in noradrenaline. We find that constrictions induced in the cerebrovasculature by increased $[Ca^{2+}]_i$ in astrocyte endfeet are generated through the phospholipase A_2–arachidonic acid pathway and 20-hydroxyeicosatetraenoic acid production. Vasoconstriction by astrocytes is a previously unknown mechanism for the regulation of CBF.

The dynamic modulation of the cerebral microvasculature by astrocytes has been difficult to assess owing to the problem of selectively stimulating astrocytes. Most stimuli that increase $[Ca^{2+}]_i$ or induce Ca^{2+} waves in astrocytes (for example, transmitter application or electrical stimulation) could also act directly on the vascular cells (that is, endothelial cells or smooth muscle cells) or neurons. We have examined the impact of increased $[Ca^{2+}]_i$ in astrocyte endfeet on the vasculature by selectively increasing $[Ca^{2+}]_i$ in astrocytes by using highly localized flash photolysis of caged Ca^{2+}, which is possible only with two-photon laser scanning
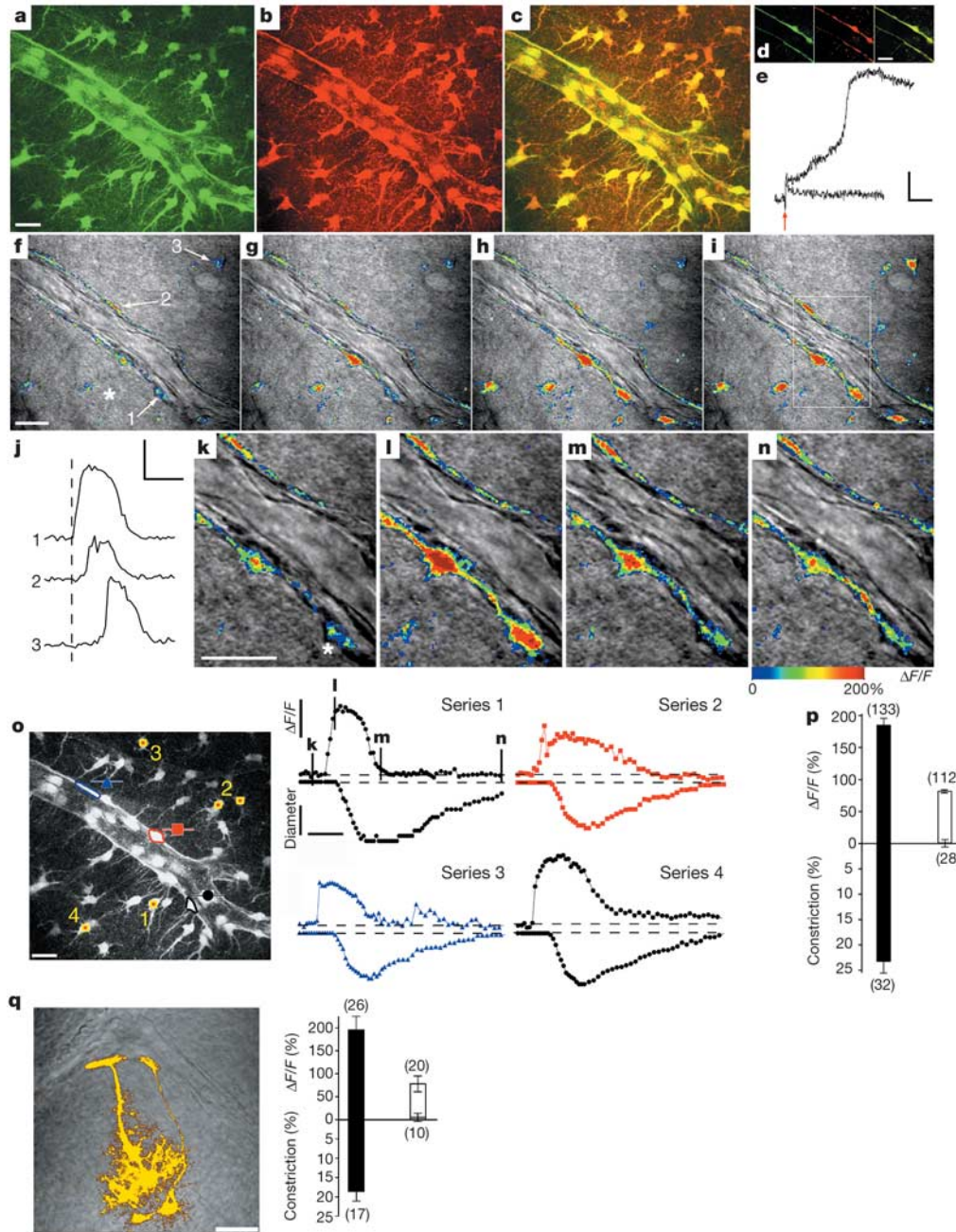

Figure 1 Two-photon photolysis of caged Ca^{2+} in identified astrocytes initiates Ca^{2+} waves that propagate to astrocyte endfeet and induce arteriole constriction. **a–d**, Two-dimensional projections showing that GFP-positive astrocytes (**a**), and the endfeet that outline an arteriole were selectively loaded with Rhod-2 (**b**; merged in **c**, single frames in **d**). **e**, Ca^{2+} uncaging in astrocytes (at red arrow) (in an area of 1 by 5 μm, bottom trace; 1 by 10 μm area, upper trace). **f–j**, Infrared-transmitted and Rhod-2 fluorescence (pseudocolour) overlay images showing the flash-induced Ca^{2+} wave (transients shown in **j**) propagates into the astrocyte endfeet at the vessel (labelled 1 and 2 in control, **f**) and precedes vessel constriction (**g–i**). The Ca^{2+} wave was induced by flashing an astrocyte cell body 10 μm below the image plane (asterisk). **k–n**, Images from the area outlined in **i** showing resting Ca^{2+} and vessel diameter under resting conditions (**k**), high endfeet $[Ca^{2+}]_i$ preceding constriction (**l**), maximal constriction/recovered Ca^{2+} (**m**) and recovery

(**n**). **o**, Repeated arteriole constrictions (series 1 to 4, measured at symbols) were evoked by uncaging in the astrocytes marked 1–4. Time points for **k–n** are shown in series 1. Asterisk in **k** indicates the endfoot measured for series 1. **p**, Summary showing astrocyte endfeet fluorescence when constriction was observed in comparison with when there was no constriction. Results are shown as means $\pm$ s.e.m. **q**, Infrared-transmitted and Fluo-3 fluorescence image (left) showing two dye-coupled astrocytes that contact the vasculature with their endfeet; whole-cell experiment summary (right) showing $\Delta F/F$ when constriction occurred in comparison with no constriction. Results are shown as means $\pm$ s.e.m. Scale bars, 20 μm (micrographs); 50% $\Delta F/F$, 1 s (**e**); 100% $\Delta F/F$, 60 s (**j**, **o**); 20% constriction (**o**). **p**, **q**, Numbers in parentheses represent n values for endfeet above the bars and arterioles below the bars.

microscopy[7,8]. Brain slices were obtained from both rats and transgenic mice in which the astrocytes were labelled with green fluorescent protein (GFP) driven by the promoter for glial fibrillary acidic protein (GFAP)[9]. Astrocytes and their endfeet were selectively loaded with the acetoxymethyl (AM) ester form of the Ca^{2+} indicator Rhod-2. Neurons and vascular elements did not load with indicator in any imaging experiments ($n = 213$ brain slices) (Fig. 1a–d; Supplementary movie 1). We co-loaded slices with the AM ester Ca^{2+} cage DMNP-EDTA to increase $[Ca^{2+}]_i$ selectively in astrocytes (Fig. 1e). The initial increase triggered Ca^{2+} waves that propagated through the astrocyte syncytium ($6.3 \pm 1.7\,\mu m\,s^{-1}$, $n = 39$ brain slices) (Fig. 1f–j; Supplementary movie 2). In control experiments ($n = 17$ brain slices), astrocytes were not co-loaded with the Ca^{2+} cage DMNP-EDTA: increases in Ca^{2+} were observed in astrocytes only at extreme laser intensities that caused non-recovering fluorescent transients and morphological damage to the astrocytes ($n = 68$ astrocytes). These increases in Ca^{2+} were isolated to the intensely illuminated astrocytes (data not shown).

The selective induction of Ca^{2+} waves in astrocytes allowed us to determine how the diameters of cerebral blood vessels were altered when Ca^{2+} waves propagated into the endfeet of astrocytes at the vessel wall. When Ca^{2+} waves reached the astrocyte endfeet and induced large increases in $[Ca^{2+}]_i$ ($\Delta F/F = 185.6 \pm 9.9\%$, $n = 133$ astrocytes in 32 brain slices), a constriction was observed in the adjacent region of the arteriole ($23.4 \pm 2.2\%$, $n = 32$ brain slices) (Fig. 1k–n; Supplementary movie 3). The peak increase in $[Ca^{2+}]_i$ in the endfeet preceded the initial onset of vessel constriction by $2.7 \pm 0.5\,s$ ($n = 32$ brain slices). Constrictions could be induced repetitively in the same arteriole with repeated Ca^{2+} waves (Fig. 1o; Supplementary movie 4). Vascular constrictions ($30.8 \pm 5.1\%$, $n = 3$) still occurred when tetrodotoxin was added to block neuronal activity. Dilation was never observed and intense laser illumination of neurons during these experiments did not induce either Ca^{2+} waves or constrictions. When Ca^{2+} waves produced changes in $[Ca^{2+}]_i$ only in the soma regions of the astrocytes without propagation into the endfeet or only small $[Ca^{2+}]_i$ changes were observed in the endfeet ($\Delta F/F = 82.5 \pm 1.24\%$; $n = 112$ astrocytes in 28 brain slices), no constriction occurred ($-0.22 \pm 0.63\%$, $n = 28$ brain slices) (Fig. 1p).

Whole-cell patch-clamp experiments were performed in astrocytes identified by morphological criteria with the use of infrared differential interference contrast (IR-DIC) optics[10] and electrophysiological properties[11] (RMP; $-84.0 \pm 1.4\,mV$ ($n = 27$)). Astrocytes were loaded with the cell-membrane-impermeant form of the Ca^{2+} cage DMNP-EDTA and the low-molecular-mass form of Fluo-3 (854 Da), that allowed for limited dye-coupling between astrocytes and fluorescence imaging in up to three astrocyte endfeet at the vessel wall (Fig. 1q). Confirming the observations above, when two-photon photolysis of the Ca^{2+} cage induced Ca^{2+} waves that propagated into the endfeet of astrocytes and induced large increases in $[Ca^{2+}]_i$ ($\Delta F/F = 196.5 \pm 28.8\%$; $n = 26$ astrocytes, 17 brain slices), a constriction was observed in the adjacent region of the arteriole ($18.6 \pm 2.4\%$, $n = 17$ brain slices; Fig. 1q). Dilation was never observed and intense laser illumination of neurons during these experiments did not induce either Ca^{2+} waves or constrictions. No constriction occurred ($-0.78 \pm 0.96\%$, $n = 10$ brain slices; Fig. 1q) when Ca^{2+} waves produced changes in $[Ca^{2+}]_i$ only in the soma regions of the astrocytes without propagation into the endfeet or when small $[Ca^{2+}]_i$ changes were observed in the endfeet ($\Delta F/F = 79.0 \pm 16\%$; $n = 20$ astrocytes, 10 brain slices).

We examined the influence of increases in endfeet $[Ca^{2+}]_i$ when the increase was widespread and involved many endfeet in comparison with when the Ca^{2+} wave propagated to only one or two endfeet. If the Ca^{2+} wave propagated along the vascular profile and caused an increase in numerous astrocyte endfeet then the constriction was equally extensive (Fig. 2a–c, g). However, if the Ca^{2+} wave propagated to only one or two endfeet and did not propagate

extensively along the arteriole, the adjacent arteriole constriction was also similarly restricted and did not propagate away from this site (Fig. 2d–g; Supplementary movie 5). The difference in the magnitude of arteriole constriction was considerable between experiments involving multiple endfeet and experiments when the increase in $[Ca^{2+}]_i$ was restricted to one or two endfeet. Arterioles constricted by $27.5 \pm 2.2\%$ ($n = 25$ brain slices) when multiple astrocyte endfeet controlled constriction compared with $9.1 \pm 0.75\%$ ($n = 7$ brain slices) when only one or two endfeet were involved (Fig. 2h). The magnitude of the endfeet $[Ca^{2+}]_i$ changes did not differ significantly: $\Delta F/F = 192.1 \pm 10.8$ (121 endfeet) and $\Delta F/F = 145.0 \pm 26.3$ (12 endfeet), respectively.

The cerebral microvasculature is densely innervated by noradrenaline projections from the locus coeruleus region that have been shown to synapse principally on astrocyte endfeet[4,5]. Activation by noradrenaline *in vivo* produces vasoconstriction and reduced CBF[2,3]. Noradrenaline also increases $[Ca^{2+}]_i$ in astrocytes[12]. Application of noradrenaline ($10\,\mu M$) in a bath evoked $[Ca^{2+}]_i$ increases in astrocyte endfeet ($\Delta F/F = 178.8 \pm 6.2$, $n = 225$ endfeet at 61 vessels) and reproducible arteriole constrictions ($29.1 \pm 1.4\%$, $n = 61$) (Supplementary Fig. 1). Arteriole constrictions never occurred without large-amplitude $[Ca^{2+}]_i$ increases in astrocyte endfeet. We examined the link between $[Ca^{2+}]_i$ increases in astrocyte endfeet and vasoconstrictions induced by noradrenaline. Local application of noradrenaline ($10\,\mu M$) increased $[Ca^{2+}]_i$ in the astrocyte endfeet ($\Delta F/F = 157.4 \pm 7.4$, $n = 31$ endfeet at 14 vessels) and produced arteriole constrictions ($26.7 \pm 1.7\%$, $n = 14$) (Fig. 3). The peak astrocyte endfeet $[Ca^{2+}]_i$ preceded the onset of arteriole constriction by $1.24 \pm 0.22\,s$ (Fig. 3). To evaluate the effect of noradrenaline in the absence of astrocytic endfeet, Ca^{2+} signalling astrocytes were loaded with the AM form of the high-affinity Ca^{2+} chelator BAPTA. Application of noradrenaline ($10\,\mu M$) in a bath in slices loaded with BAPTA-AM ($100\,\mu M$) evoked minimal
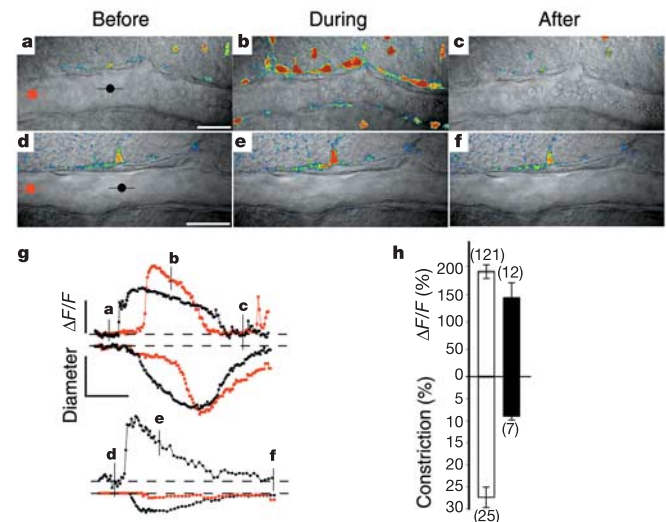

Figure 2 The extent of vascular constrictions was related to the number of endfeet showing increased $[Ca^{2+}]_i$. Vascular constrictions were greater and more widespread when $[Ca^{2+}]_i$ increased in numerous endfeet (**a–c**) compared with only one endfoot (**d–f**). **a–g**, IR-transmitted and Rhod-2 fluorescence (pseudocolour) overlay images (**a–f**) and measurements (**g**, taken at the symbols) showing two different vessels and their associated endfeet $[Ca^{2+}]_i$ before, during and after maximal increases in endfeet $[Ca^{2+}]_i$ resulting from Ca^{2+} waves. Scale bars **a–f**, 30 μm. Image time points (**a–f**) are marked on the Ca^{2+} transients. Scale bars **g**, 100% $\Delta F/F$, 20% diameter change, 60 s. **h**, $[Ca^{2+}]_i$ increases in multiple endfeet (non-filled bars) in comparison with one or two endfeet (filled bars) and associated constrictions. Results are shown as means $\pm$ s.e.m. Numbers in parentheses represent n values for endfeet above the bars and arterioles below the bars.

Ca^{2+} increases in astrocyte endfeet ($\Delta F/F = 19.8 \pm 6.4$, $n = 55$ endfeet at nine vessels) and small arteriole constrictions ($9.9 \pm 2.5\%$, $n = 9$) (Supplementary Fig. 2). It is unlikely that BAPTA was in smooth muscle cells because we never saw any indication of loading in smooth muscle cells with AM dyes, and direct electrical stimulation of arterioles in these experiments could still induce constriction. It is possible that noradrenaline might have additional direct actions on the vessels themselves.

The time delay of several seconds between the increase in $[Ca^{2+}]_i$ in the endfeet and the vascular constriction suggests the formation and release of an intercellular second messenger that diffuses from the astrocyte endfoot to the vascular cells. We tested the involvement of the Ca^{2+}-sensitive phospholipase A_2 (PLA_2), which is principally expressed in astrocytes[13] and causes the release of arachidonic acid from increased $[Ca^{2+}]_i$[14]. Blocking PLA_2 with $100\,\mu M$ methyl arachidonyl fluorophosphonate (MAFP)[15] eliminated vascular constrictions ($-1.3 \pm 3.1\%$, $n = 6$; Fig. 4a). The major vasoconstrictive metabolite 20-hydroxyeicosatetraenoic acid (20-HETE)[16] is generated copiously in cerebrovascular smooth muscle cells by CYP4A, a cytochrome P450 (CYP450) enzyme subtype, in response to elevated arachidonic acid concentrations[17]. 20-HETE blocks calcium-activated K^+ channels in smooth muscle cells, leading to depolarization, increased Ca^{2+} influx and contraction[16]. Inhibiting 20-HETE formation with the selective CYP4A

inhibitor HET0016 (ref. 18) ($100\,\mu M$) blocked vascular constrictions ($0.1 \pm 0.1\%$, $n = 8$; Fig. 4a). A recent study[19] indicated that Ca^{2+} increases in astrocytes might induce vasodilation. However, in that study most slices were preincubated in N^G-nitro-L-arginine methyl ester (L-NAME) to block NO formation and preconstrict blood vessels[19]. In contrast, we found that in untreated control slices the mGluR agonist 1-aminocyclopentane-trans-1,3-dicarboxylic acid (t-ACPD; $100\,\mu M$), increased Ca^{2+} in astrocyte endfeet and induced robust vascular constrictions ($22.3 \pm 1.6\%$, $n = 6$, Fig. 4a). Incubating slices in L-NAME ($100\,\mu M$) abolished the t-ACPD induced constrictions that we observed in control conditions and induced a small dilation ($-13.2 \pm 7.8\%$, $n = 6$, Fig. 4a). We therefore propose that, under physiological conditions, increased $[Ca^{2+}]_i$ in astrocyte endfeet activates PLA_2, inducing the formation and release of arachidonic acid, which is converted to 20-HETE by CYP450 enzymes in smooth muscle cells to induce contraction
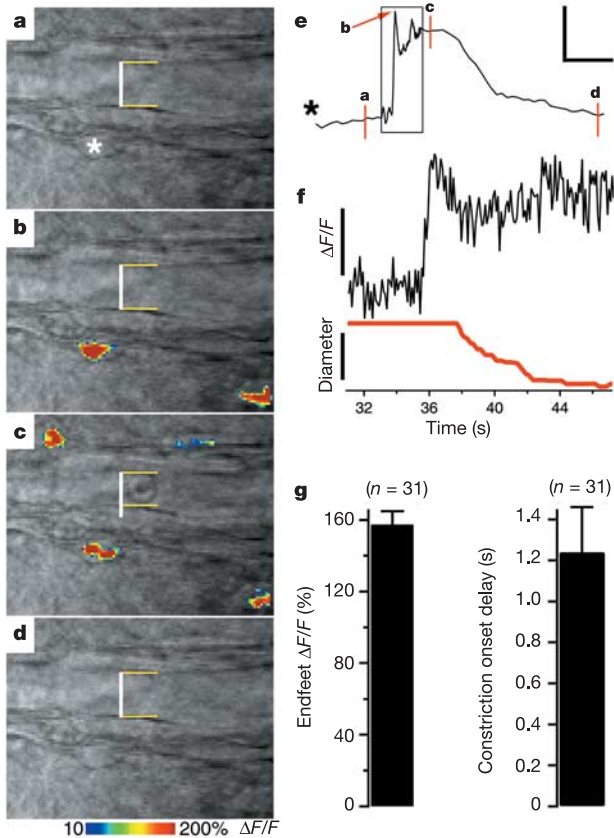

Figure 3 Noradrenaline-induced Ca^{2+} elevations in astrocyte endfeet precede the onset of vessel constriction. **a–e**, Overlay images (**a–d**) showing the arteriole and endfeet $[Ca^{2+}]_i$ responses to noradrenaline ($10\,\mu M$). Peak astrocyte endfoot response (asterisk, timecourse in **e** with frame times) precedes the onset of arteriole constriction. The control diameter was $11\,\mu m$. **f**, Expanded timecourse from **e** (boxed area) showing endfoot $[Ca^{2+}]_i$ increases before vessel constriction. Scale bars, 20 s for **e**, 100% $\Delta F/F$ for **e** and **f**, 20% diameter change for **f**. **g**, Average amplitude of endfeet $[Ca^{2+}]_i$ in noradrenaline and the time between the peak astrocyte endfeet $[Ca^{2+}]_i$ and arteriole constriction onset. Results are shown as means ± s.e.m.
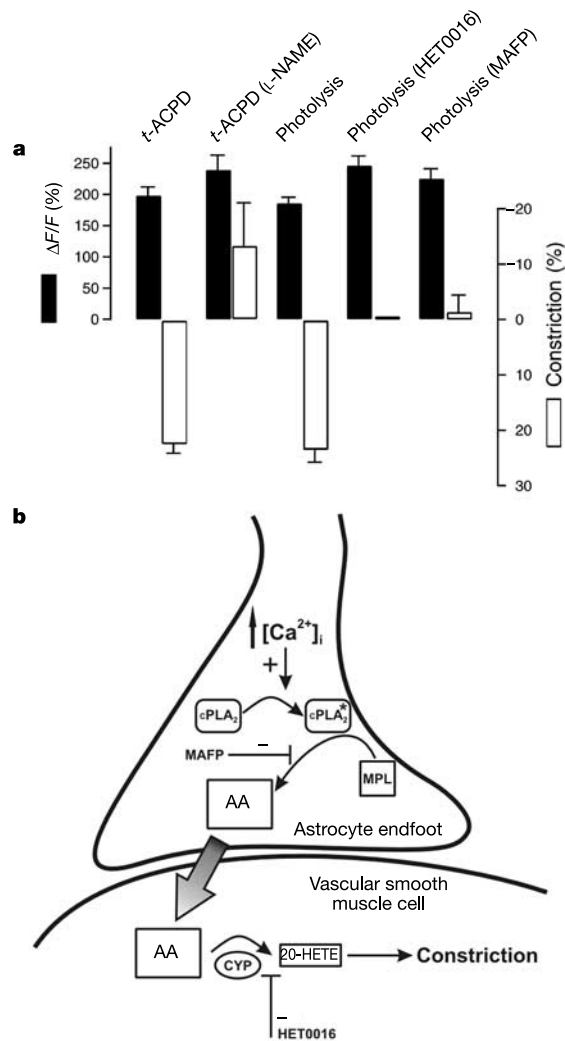

Figure 4 Increased $[Ca^{2+}]_i$ in astrocyte endfeet causes cerebrovascular constrictions. **a**, Summary showing Rhod-2 $\Delta F/F$ in endfeet and associated constriction under several conditions. mGluR receptor activation by t-ACPD is compared in control versus with L-NAME to block NO generation. Ca^{2+} photolysis is compared in control conditions versus with CYP4A inhibition (HET0016), or with phospholipase A_2 inhibition (MAFP). Results are shown as means ± s.e.m. **b**, The proposed mechanism of astrocyte endfoot Ca^{2+}-induced vascular constrictions. Increased $[Ca^{2+}]_i$ in the astrocyte endfeet activates cytosolic Ca^{2+}-activated PLA_2 and increases arachidonic acid (AA) formation from membrane phospholipids (MPL). AA freely diffuses to smooth muscle cells to be converted to 20-HETE by CYP4A and thus to induce vascular constrictions.

(Fig. 4b). CYP450 enzymes and 20-HETE formation are inhibited by nitric oxide[16]. Generation of nitric oxide by neuronal activity might contribute to vasodilation by preventing the vasoconstriction induced by arachidonic acid released from astrocytes.

We conclude that astrocyte Ca^{2+} waves cause vascular constrictions when the endfeet participate in the Ca^{2+} wave. This represents a previously unknown mechanism of CBF regulation. Vasoactive neuronal projections that control CBF and extend the upper range of autoregulation[20] might mediate these actions through Ca^{2+}-dependent processes in astrocyte endfeet. Finally, these observations provide a link between increased $[Ca^{2+}]_i$ in astrocytes and haemodynamic pathology. Increased $[Ca^{2+}]_i$ in astrocytes during spreading depression[21] might cause the associated phase of vasoconstriction[22]. During a stroke, the ischaemic insult increases astrocyte $[Ca^{2+}]_i$ (ref. 23), which might induce vascular constrictions to decrease CBF further and exacerbate infarct damage. Astrocyte $[Ca^{2+}]_i$ signalling might therefore be a novel therapeutic target for treatment of stroke and migraine. □

Methods

Slice preparation and AM-ester loading

Brain slices were obtained from both rats and GFAP/GFP transgenic mice (strain FVB/N-TgN(GFAPGFP)14Mes; Jackson Labs)[9] aged 13–18 days postnatal, as described previously[21]. Slices were stored at room temperature (20 to 22 °C) for 1 h before the loading of dye/Ca^{2+} chelator in an oxygenated artificial cerebrospinal fluid (aCSF) containing (in mM): NaCl 126, KCl 2.5 or 4.2, NaHCO$_3$ 26, glucose 10, MgCl$_2$ 2, NaH$_2$PO$_4$ 1.25 and CaCl$_2$ 2. Astrocytes were co-loaded with the Ca^{2+} indicator Rhod-2-AM (10 μM) and the Ca^{2+} cage DMNP-EDTA-AM (10 μM) (Molecular Probes, Eugene, Oregon) for 1 h (DMSO concentration 0.3%). For the Ca^{2+} chelation experiments, the astrocytes were co-loaded with the Ca^{2+} indicator Rhod-2-AM (10 μM) and the membrane-permeable (AM ester) form of the Ca^{2+} chelator BAPTA (100 μM) (Molecular Probes) for more than 1 h (DMSO concentration 0.3%) and the multidrug resistance protein transport inhibitor probenicid (1–3 mM; Sigma, Oakville, Ontario). Slices were transferred to a recording chamber and perfused with oxygenated aCSF at a rate of 1–3 ml min^{-1} and maintained at either 25 ± 0.5 or 33 ± 0.5 °C with an inline heater (Warner Instruments). In some experiments ($n = 18$) the extracellular $[K^+]$ was increased to 4.2 mM to ensure that vascular responses were not altered with higher $[K^+]$.

Two-photon imaging and photolysis

We performed imaging with a two-photon laser-scanning microscope (Zeiss LSM510-Axioskop-2 fitted with a 40X-W/0.80 numerical aperture objective lens) directly coupled to a Mira Ti:sapphire laser (∼100-fs pulses, 76 MHz, pumped by a 5 W Verdi laser; Coherent). GFP and the Rhod-2 fluorophore, which have large two-photon absorption cross-sections[24], were excited at 835–840 nm and epifluorescence was detected with external detectors with 510-nm (40 nm bandpass) and 605-nm (55 nm bandpass) filters. For two-photon photolysis within single or multiple astrocytes we tuned the Ti:sapphire laser to 730 nm for maximum Ca^{2+} uncaging of DMNP-EDTA[8] and excitation of Rhod-2. Laser intensities were the lowest possible for uncaging. Flash durations between 3 and 10 ms within single astrocytes produced repeatable small transients. The laser intensity was carefully increased beyond the point for the initial transient event until a large Ca^{2+} transient characteristic of internal release occurred within the astrocyte that then induced a Ca^{2+} wave that propagated throughout the astrocyte network. Because of the highly nonlinear nature of two-photon photolysis of caged Ca^{2+} (ref. 8), no uncaging occurs during Rhod-2 fluorescence acquisition, in which laser intensity was typically one-tenth of the intensity necessary for photolysis.

Whole-cell patch recording

Astrocytes, identified using IR-DIC optics, were recorded in whole-cell current-clamp mode with an Axopatch 200B amplifier. Pipette (3–7 MΩ) solution (pH 7.2–7.4) contained (in mM): potassium gluconate 130, KCl 10, HEPES 10, NaATP 4, TrisGTP 0.3, Fluo-3 pentaammonium salt (854 Da; Molecular Probes) 0.1–0.3, and DMNP-EDTA 2 (the cell-membrane-impermeant form of the Ca^{2+} cage; Molecular Probes) loaded with Ca^{2+} (60–75%). Fluo-3 fluorescence was detected with a 510-nm (40 nm bandpass) emission filter and 488-laser line excitation (Zeiss LSM510).

Analysis of Ca^{2+} signals and arteriole diameter

Arterioles (lumen diameter 15.4 ± 0.7 μm) were identified with IR-DIC optics and chosen on the basis of their diameter, appearance of smooth muscle cells and healthy appearance over an extended region. Although blood vessels in brain slices do not experience the same shear stresses as they do in vivo, repeatable constrictions could be induced. Vessel diameter changes were imaged by acquiring 730-nm-wavelength laser transmission with an external photomultiplier simultaneously with the Rhod-2 and Fluo-3 fluorescence. Image series were analysed off-line, and luminal diameter measurements were made at multiple sites along the vessel and quantified with Zeiss LSM (version 2.8) software and custom-made autotracking software (Diamtrak, developed by

T. O. Neild). Fluorescence signals were defined as $\Delta F/F = [(F_1 - B_1) - (F_0 - B_0)]/(F_0 - B_0)$, where F_1 and F_0 are fluorescence in the astrocyte endfoot at any given time point and at the beginning of the experiment respectively, and B_1 and B_0 are the background fluorescence at the same time point and at the beginning of the experiment respectively. Background values were taken from an adjacent area located at least 10 μm from imaged areas. Results are shown as means ± s.e.m.

Drug application experiments

N-Hydroxy-N'-(4-butyl-2-methylphenyl)-formamidine (HET0016, a gift from Taisho Pharmaceutical Co.) the inhibitor of 20-HETE, and MAFP, the inhibitor of PLA$_2$, were applied by incubating brain slices for 1–2 h before transfer to the perfusion and imaging chamber. t-ACPD (100 μM) and noradrenaline (10 μM in aCSF) were applied in a bath. Noradrenaline was also locally applied through a manipulator-controlled pipette (∼2 MΩ) by a picospritzer with less than 1 lb in^{-2} air pressure. Noradrenaline was prepared freshly before each application. Arteriole transmitted and astrocyte endfeet fluorescence images were acquired at 85–147-ms frame rates. The delay in constriction onset was defined as the difference between the initial time point of peak astrocyte endfeet fluorescence and the initial arteriole constriction event.

1. Chaigneau, E., Oheim, M., Audinat, E. & Charpak, S. Two-photon imaging of capillary blood flow in olfactory bulb glomeruli. *Proc. Natl Acad. Sci. USA* **100**, 13081–13086 (2003).
2. Raichle, M. E., Hartman, B. K., Eichling, J. O. & Sharpe, L. G. Central noradrenergic regulation of cerebral blood flow and vascular permeability. *Proc. Natl Acad. Sci. USA* **72**, 3726–3730 (1975).
3. Goadsby, P. J. & Edvinsson, L. in *Cerebral Blood Flow and Metabolism* (ed. Krause, D. N.) 172–188 (Lippincott Williams & Wilkins, Philadelphia, 2002).
4. Cohen, Z., Molinatti, G. & Hamel, E. Astroglial and vascular interactions of noradrenaline terminals in the rat cerebral cortex. *J. Cereb. Blood Flow Metab.* **17**, 894–904 (1997).
5. Paspalas, C. D. & Papadopoulos, G. C. Ultrastructural relationships between noradrenergic nerve fibers and non-neuronal elements in the rat cerebral cortex. *Glia* **17**, 133–146 (1996).
6. Simard, M., Arcuino, G., Takano, T., Liu, Q. S. & Nedergaard, M. Signaling at the gliovascular interface. *J. Neurosci.* **23**, 9254–9262 (2003).
7. Soeller, C. & Cannell, M. B. Two-photon microscopy: imaging in scattering samples and three-dimensionally resolved flash photolysis. *Microsc. Res. Tech.* **47**, 182–195 (1999).
8. Brown, E. B., Shear, J. B., Adams, S. R., Tsien, R. Y. & Webb, W. W. Photolysis of caged calcium in femtoliter volumes using two-photon excitation. *Biophys. J.* **76**, 489–499 (1999).
9. Zhuo, L. *et al.* Live astrocytes visualized by green fluorescent protein in transgenic mice. *Dev. Biol.* **187**, 36–42 (1997).
10. Kang, J. & Nedergaard, M. in *Imaging Neurons: A Laboratory Manual* (ed. Konnerth, A.) 42.1–42.11 (Cold Spring Harbor Laboratory Press, Cold Spring Harbor, New York, 2000).
11. Walz, W. & MacVicar, B. Electrophysiological properties of glial cells: comparison of brain slices with primary cultures. *Brain Res.* **443**, 321–324 (1988).
12. Duffy, S. & MacVicar, B. A. Adrenergic calcium signaling in astrocyte networks within the hippocampal slice. *J. Neurosci.* **15**, 5535–5550 (1995).
13. Farooqui, A. A., Yang, H. C., Rosenberger, T. A. & Horrocks, L. A. Phospholipase A$_2$ and its role in brain tissue. *J. Neurochem.* **69**, 889–901 (1997).
14. Katsuki, H. & Okuda, S. Arachidonic acid as a neurotoxic and neurotrophic substance. *Prog. Neurobiol.* **46**, 607–636 (1995).
15. Street, I. P. *et al.* Slow- and tight-binding inhibitors of the 85-kDa human phospholipase A2. *Biochemistry* **32**, 5935–5940 (1993).
16. Roman, R. J. P-450 metabolites of arachidonic acid in the control of cardiovascular function. *Physiol. Rev.* **82**, 131–185 (2002).
17. Gebremedhin, D. *et al.* Production of 20-HETE and its role in autoregulation of cerebral blood flow. *Circ. Res.* **87**, 60–65 (2000).
18. Miyata, N. *et al.* HET0016, a potent and selective inhibitor of 20-HETE synthesizing enzyme. *Br. J. Pharmacol.* **133**, 325–329 (2001).
19. Zonta, M. *et al.* Neuron-to-astrocyte signaling is central to the dynamic control of brain microcirculation. *Nature Neurosci.* **6**, 43–50 (2003).
20. Chillon, J. M. & Baumbach, G. L. in *Cerebral Blood Flow and Metabolism* (ed. Krause, D. N.) 395–412 (Lippincott Williams & Wilkins, Philadelphia, 2002).
21. Basarsky, T. A., Duffy, S. N., Andrew, R. D. & MacVicar, B. A. Imaging spreading depression and associated intracellular calcium waves in brain slices. *J. Neurosci.* **18**, 7189–7199 (1998).
22. Dreier, J. P. *et al.* Ischaemia triggered by spreading neuronal activation is inhibited by vasodilators in rats. *J. Physiol. (Lond.)* **531**, 515–526 (2001).
23. Duffy, S. & MacVicar, B. A. In vitro ischemia promotes calcium influx and intracellular calcium release in hippocampal astrocytes. *J. Neurosci.* **16**, 71–81 (1996).
24. Xu, C., Zipfel, W., Shear, J. B., Williams, R. M. & Webb, W. W. Multiphoton fluorescence excitation: new spectral windows for biological nonlinear microscopy. *Proc. Natl Acad. Sci. USA* **93**, 10763–10768 (1996).